Cancer Research

Effective Photothermal Chemotherapy Using Doxorubicin-Loaded Gold Nanospheres That Target EphB4 Receptors in Tumors

Jian You[1], Rui Zhang[2], Chiyi Xiong[2], Meng Zhong[2], Maritess Melancon[2], Sanjay Gupta[3], Alpa M. Nick[4,6], Anil K. Sood[4,5,6], and Chun Li[2,6]

Abstract

Photothermal ablation (PTA) is an emerging technique that uses near-infrared (NIR) laser light–generated heat to destroy tumor cells. However, complete tumor eradication by PTA therapy alone is difficult because heterogeneous heat distribution can lead to sublethal thermal dose in some areas of the tumor. Successful PTA therapy requires selective delivery of photothermal conducting nanoparticles to mediate effective PTA of tumor cells, and the ability to combine PTA with other therapy modalities. Here, we synthesized multifunctional doxorubicin (DOX)-loaded hollow gold nanospheres (DOX@HAuNS) that target EphB4, a member of the Eph family of receptor tyrosine kinases overexpressed on the cell membrane of multiple tumors and angiogenic blood vessels. Increased uptake of targeted nanoparticles T-DOX@HAuNS was observed in three EphB4-positive tumors both *in vitro* and *in vivo*. *In vivo* release of DOX from DOX@HAuNS, triggered by NIR laser, was confirmed by dual-radiotracer technique. Treatment with T-DOX@HAuNS followed by NIR laser irradiation resulted in significantly decreased tumor growth when compared with treatments with nontargeted DOX@HAuNS plus laser or HAuNS plus laser. The tumors in 6 of the 8 mice treated with T-DOX@HAuNS plus laser regressed completely with only residual scar tissue by 22 days following injection, and none of the treatment groups experienced a loss in body weight. Together, our findings show that concerted chemo-photothermal therapy with a single nanodevice capable of mediating simultaneous PTA and local drug release may have promise as a new anticancer therapy. *Cancer Res; 72(18); 4777–86. ©2012 AACR.*

Introduction

Photothermal ablation (PTA) therapy is a recently developed technique that uses near-infrared (NIR) laser light–generated heat to destroy tumor cells. PTA has gained popularity recently because a specific amount of photoenergy is delivered directly into the tumor mass without causing systemic effects, thus promising minimally invasive intervention as an alternative to surgery (1, 2). However, PTA therapy alone is unlikely to kill all tumor cells because the heat distribution is nonuniform, especially in areas peripheral to large blood vessels where heat can be rapidly dissipated by circulating blood. To improve the efficacy and tumor selectivity of laser-induced PTA, light-absorbing photothermal conducting nanoparticles are introduced. In principle, NIR laser–modulated photothermal effects can not only enable PTA of tumor cells but also trigger release of anticancer agents. Such a multimodal approach, which permits simultaneous PTA therapy and chemotherapy, should provide an opportunity for complete eradication of tumor cells.

Hollow gold nanospheres (HAuNS) are novel gold nanostructures ideally suited for PTA because of their unique combination of small size (30–50 nm), biocompatibility, and strong and tunable absorption in the entire NIR region (3, 4). Owing to their hollow interior, exceptionally high doxorubicin (DOX) payload to HAuNS (up to 60% by weight, 4-fold of the payload achievable with solid gold nanoparticles of the similar size) could be achieved with HAuNS (5). To maximize the therapeutic efficacy of DOX-loaded HAuNS (DOX@HAuNS), it is essential that DOX@HAuNS are selectively delivered to the tumor. The Eph receptors constitute the largest known family of receptor tyrosine kinases and have been reported to control various pathological processes, including tumor progression and angiogenesis, chronic pain following tissue damage, inhibition of nerve regeneration after spinal cord injury, and human congenital malformations (6–15). Overexpression of EphB4 has also been observed in numerous tumor types, including prostate, breast, bladder, lung, colon, gastric, and ovarian cancers (6–8, 14–18). Knocking down EphB4 can result in inhibition of tumor growth, induction of apoptosis, and

Authors' Affiliations: [1]College of Pharmaceutical Sciences, Zhejiang University, Hangzhou, PR China; Departments of [2]Experimental Diagnostic Imaging, [3]Diagnostic Radiology, [4]Gynecologic Oncology, and [5]Cancer Biology, [6]Center for RNA Interference and Non-Coding RNA, The University of Texas MD Anderson Cancer Center, Houston, Texas

Note: Supplementary data for this article are available at Cancer Research Online (http://cancerres.aacrjournals.org/).

Corresponding Author: Chun Li, Department of Experimental Diagnostic Imaging, Unit 59, The University of Texas MD Anderson Cancer Center, Houston, TX 77030. Phone: 713-792-5182; Fax: 713-794-5456; E-mail: cli@mdanderson.org

doi: 10.1158/0008-5472.CAN-12-1003

reduction in tumor vascularity (18). Therefore, EphB4 is a particularly promising target for tumor-specific delivery of DOX@HAuNS.

We have recently reported the first micro-positron emission tomography (PET) imaging agent for detection of EphB4 in cancer cells (19). This PET imaging agent was developed on the basis of a 14-mer peptide identified by phage display technology (15). The parent peptide TNYLFSPNGPIARAW (designated as TNYL-RAW) and its derivatives displayed high binding affinity to EphB4, with an equilibrium dissociation constant (K_d) values of 1.98 to 23 nmol/L (19). Cyclic peptide c(TNYL-RAW) is a second-generation EphB4-binding antagonist with improved plasma stability and high-receptor binding affinity. Here, we show for the first time that using c(TNYL-RAW) as a homing ligand, DOX@HAuNS were selectively targeted to EphB4-positive tumors, and that concerted chemo-photothermal therapy mediated by EphB4-targeting DOX@HAuNS induced remarkable antitumor efficacy with reduced systemic toxicity. Our results support the concept of integrating multiple functions into a single nanodevice to mediate simultaneous PTA and local drug release.

Materials and Methods

Synthesis of SH-PEG-c(TNYL-RAW)

The heterofunctional PEG linker SATA-PEG-CONHS containing a protected sulfohydryl group (*S*-acetylthioacetate, SATA) and NHS activated ester on each end of the PEG chain was first synthesized. Briefly, NH_2-PEG-COOH (0.5 g, 0.25 mmol) and 1.2 equivalent *N*-succinimidyl-*S*-acetylthioacetate (SATA) were dissolved in 2 mL anhydrous DCM, and then 3 equivalents of dry DIPEA was added dropwise. The reaction solution was stirred at room temperature overnight. After all organic solvent was removed under a vacuum, the crude product was purified by gel filtration with PD-10 column. The collected aqueous solution was lyophilized to yield SATA-PEG-COOH, which was further activated with 1-ethyl-3-[3-dimethylaminopropyl]carbodiimide (EDC) and NHS to make SATA-PEG-CONHS. c(TNYL-RAW) was synthesized on solid support (Supplementary Information). The peptide was conjugated to SATA-PEG_{5000}-CONHS in a 1:1 molar ratio in DCM to obtain SATA-PEG-c(TNYL-RAW). The product was purified by PD-10 column and then treated with 0.5 M NH_2OH to obtain SH-PEG-c(TNYL-RAW) before conjugation with HAuNS.

Synthesis of DOX-loaded, c(TNYL-RAW)–conjugated HAuNS

HAuNS were synthesized according to a previously reported method (5). Briefly, cobalt nanoparticles were first synthesized by deoxygenating deionized water containing 4.5 mL of 1 mol/L sodium borohydride, 2.8 mL of 0.1 mol/L sodium citrate, and 1.0 mL of 0.4 mol/L cobalt chloride. After chloroauric acid was added into the solution containing cobalt nanoparticles, the cobalt immediately reduced the gold ions onto the surface of the nanoparticles and was simultaneously oxidized to cobalt oxide. Any remaining cobalt was further oxidized by air, resulting in the final product, HAuNS. The size of the HAuNS was determined using dynamic light scattering on a Brookhaven 90Plus particle size analyzer. The UV-visible spectra were recorded on a Beckman Coulter DU-800 UV-visible spectrometer. The morphology of the HAuNS was examined using a JEM 1010 transmission electron microscope (JEOL).

To obtain c(TNYL-RAW)-conjugated HAuNS, SH-PEG-c(TNYL-RAW) (50 nmol) was mixed with 1.0 mL HAuNS solution [200 optical density (OD), 5.0 mg/mL] and stirred overnight. Then, SH-PEG (3 μmol) was added to the solution. After another overnight stirring, c(TNYL-RAW)-conjugated HAuNS was purified on a PD-10 column.

For DOX loading, free DOX (5 mg) in water (5 mL) was added to c(TNYL-RAW)-HAuNS (40 OD) in 5 mL of 2.8 mmol/L citrate solution, and the mixture was stirred at room temperature for 24 hours. The resulting DOX-loaded c(TNYL-RAW)-HAuNS (T-DOX@HAuNS) were purified by 3 repeated centrifugation and washing steps.

Cell uptake of HAuNS

Cells were transferred and cultured onto 20-mm glass coverslips in a 24-well plate and allowed to grow for 2 days. The medium was replaced with 1 mL of fresh culture medium containing T-DOX@HAuNS. After incubation for 2 hours, cell nuclei were stained with 4′, 6-diamidino-2-phenylindole. The cell monolayer on the coverslip was removed, repeatedly rinsed with PBS, and then mounted for microscopic examination. The cellular fluorescence and dark-field light scattering images were examined under a Zeiss Axio Observer Z1 fluorescence microscope equipped with a dark-field condenser.

Quantitative cellular uptake was determined using ^{111}In-labeled nanoparticles. Hey and A549 cells ($\sim 1 \times 10^6$/dish) were cultured in 60 $\times$15 mm^2 dishes. Cells were incubated with ^{111}In-labeled T-DOX@HAuNS or ^{111}In-labeled DOX@HAuNS (1.5 μCi/dish) for 3 hours at room temperature in culture medium lacking FBS and phenol red. For the blocking experiments, cells were incubated with free c(TNYL-RAW) (1.0 μmol/L) for 0.5 hours and then with ^{111}In-labeled T-DOX@HAuNS or ^{111}In-labeled DOX@HAuNS under the same conditions. Cells were rinsed 5 times with PBS (pH 7.4). After the PBS was removed, the cells were scraped off the dish, suspended in PBS, and the radioactivity of the cell suspension was then measured with a gamma counter. Protein concentration in cell suspension was quantified using the Bio-Rad protein assay kit. The data are expressed as radioactivity (dpm/μg protein).

Cytotoxicity

Cytotoxicity was measured using an MTT assay according to the manufacturer's suggested procedures. EphB4-positive A2780 cells and EphB4-negative A549 cells were exposed to free DOX, DOX@HAuNS, or T-DOX@-HAuNS for 72 hours. The data are expressed as the percentage of surviving cells and are reported as the mean values of 3 measurements.

Pharmacokinetics and biodistribution

All animal studies were carried out under Institutional Animal Care and Use Committee–approved protocols. For the pharmacokinetic analysis, 8 healthy female Swiss mice (22–25 g; Charles River Laboratories) for each group were each injected intravenously with a dose of either ^{111}In-labeled

T-DOX@-HAuNS or ^{111}In-labeled DOX@HAuNS [both 20 μCi, 1.0 mg/mL (40 OD) in 0.2 mL citrate–buffered solution]. At predetermined intervals up to 48 hours, blood samples (10 μL) were taken from the tail vein, and the radioactivity of each sample was measured with a gamma counter. The percentage of the injected dose per gram of blood (%ID/g) was calculated. The blood pharmacokinetic parameters for the radiotracer were analyzed using a noncompartmental model with WinNonlin 5.0.1 software (Pharsight).

To investigate the *in vivo* distribution of T-DOX@-HAuNS, we intravenously injected female nude mice (Harlan) bearing 6 to 8 mm subcutaneous A2780, MDA-MB-231, or Hey tumors with ^{111}In-labeled T-DOX@-HAuNS or ^{111}In-labeled DOX@HAuNS (20 μCi/mouse in 0.2 mL). For the blocking studies, the mice were intravenously injected with a mixture of ^{111}In-labeled T-DOX@-HAuNS (20 μCi/mouse in 0.2 mL) and an excess of free c(TNYL-RAW) (0.3 μmol). Mice were killed at 24 hours after injection. Various tissues, including tumors, were collected and weighted. The radioactivity for each sample was measured with a gamma counter. Uptake of nanoparticles in various tissues was calculated as %ID/g.

Single-photon emission computed tomography imaging

Mice bearing subcutaneous Hey tumors were intravenously injected with ^{111}In-labeled T-DOX@HAuNS or DOX@HAuNS [8.0 mCi/kg, 0.525 mg/mL (25 OD)]. For the blocking studies, mice were injected intravenously with a mixture of ^{111}In-labeled DOX@c(TNYL-RAW)-HAuNS and free c(TNYL-RAW) (0.3 μmol). The mice were placed in a prone position and anesthetized with 0.5% to 2.0% isoflurane gas (Iso-Thesia) in oxygen. Single-photon emission computed tomography (SPECT) images were generated at 24 hours after injection. After imaging, the mice were killed and their tumors were removed. The tumors were snap-frozen and cut into 5-μm slices that were then used for autoradiography analysis on a Fujifilm FLA-5100 imaging system.

NIR laser–triggered DOX release *in vivo*

For measuring the photothermal effect of T-DOX@HAuNS, mice bearing Hey tumors were injected intravenously with saline (5.0 mL/kg) or T-DOX@-HAuNS (5.0 mL/kg of 50 OD HAuNS). At 24 hours after injection, the tumor was irradiated with an NIR laser (3W/cm^2) for 5 minutes (Diomed 15 Plus) through the skin surface. Temperature was measured with 2 thermocouples inserted into the tumor. Care was taken to ensure that the thermocouple was not directly exposed to the laser beam.

The DOX release mediated by the photothermal effect in the Hey tumors was studied using ^{111}In- and ^{3}H-labeled T-DOX@-HAuNS, in which the HAuNS were labeled with ^{111}In and the DOX with ^{3}H. Tumors were irradiated by NIR laser light (3 W/cm^2 for 5 minutes) at 1 hour after intratumoral injection of the dual-labeled nanoparticles (^{3}H: 10 μCi; ^{111}In: 20 μCi) into the center of the tumor. The mice were killed 5 minutes after laser irradiation, and the tumors were removed, snap-frozen, and sliced into 10-μm sections. Injected tumors that did not receive NIR laser treatment were similarly prepared and used as controls.

The radioactive signals from ^{111}In and ^{3}H were detected using a Fujifilm FLA-5100 imaging system. Briefly, the sections of the tumors were exposed to phosphorous screen film (an SR imaging plate) for 15 minutes at −10°C, and the ^{111}In autoradiograph was obtained by scanning the film. After the ^{111}In was completely decayed (stored at −80°C for 5 weeks), the same sections were exposed to phosphorous screen film (a TR imaging plate) for 3 days at −10°C, and the ^{3}H autoradiograph was obtained by scanning the film. Concurrently, control specimens from tumors that were not laser treated were subjected to the same procedures. The autoradiographic distribution of ^{111}In-HAuNS and ^{3}H-DOX was compared by overlaying the 2 autoradiograms.

Antitumor activity *in vivo*

Hey tumors were generated by subcutaneous injection of Hey cells (5.0×10^6 cells/mouse). When the mean tumor volume reached approximately 200 mm^3, mice were divided into 4 groups consisting of 6 to 8 mice each. Mice in groups 1 through 4 were injected intravenously with saline ($n = 6$, 5.0 mL/kg), HAuNS ($n = 6$, 5.0 mL/kg of 1.25 mg HAuNS/mL solution), DOX@HAuNS ($n = 7$, 10 mg equivalent DOX/kg, 5.0 mL/kg of 1.25 mg HAuNS/mL solution), and T-DOX@HAuNS ($n = 8$, 10 mg equivalent DOX/kg, 5.0 mL/kg of 1.25 mg HAuNS/mL solution), respectively. All mice received NIR laser irradiation through the skin surface at 24 hours postinjection (2.0 W/cm^2 for 3 minutes). The tumor dimensions were measured with a caliper, and the tumor volume was calculated according to the following equation: volume = (tumor length) × (tumor width)^2/2. At the end of the experiment (when the tumor size reached >1500 mm^3 or 22 days after initial injection, whichever came first), mice were killed by CO_2 asphyxiation, and the tumors were collected and weighed. Parts of the tumors were fixed in formalin and cut into 5-μm slices for hematoxylin and eosin staining. Body weight was measured weekly to assess systemic toxicity.

Statistics

Pharmacokinetic data were analyzed using noncompartmental WinNonlin method. Statistical analysis was conducted using the SYSTAT program. *P* values were obtained using the 2-sample *t* test. For cellular uptake, biodistribution, and antitumor activity data, statistic analyses were conducted by ANOVA, with $P < 0.05$ considered to be statistically significant.

Results

Synthesis and characterization of EphB4-targeted T-DOX@HAuNS

Before carrying out efficacy studies, we conducted a number of experiments to fully characterize the targeted DOX@HAuNS system for *in vivo* delivery. The average diameter of the HAuNS was 36.8 ± 1.6 nm, as determined by dynamic light scattering. Transmission electron microscopy (TEM) confirmed that the HAuNS consisted of a thin gold shell (~4 nm thickness) with a hollow interior. The extinction spectrum showed that the plasma resonance peak for HAuNS was approximately 800 nm (Supplementary Fig. S1).

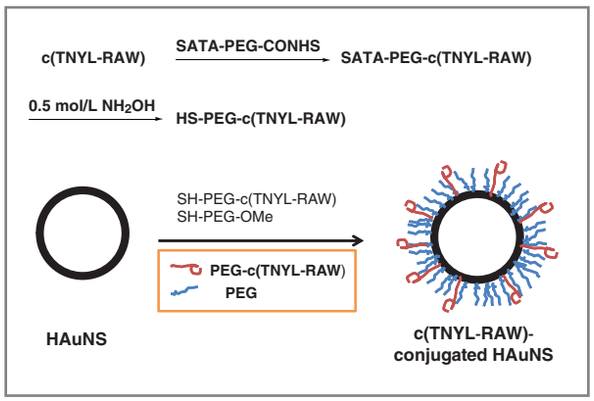

Figure 1. Reaction scheme for the synthesis of SH-PEG-c(TNYL-RAW) and its conjugation to HAuNS.

The targeting ligand cyclic peptide c(TNYL-RAW) is a second-generation EphB4–binding antagonist. The peptide had K_d of 4.4 nmol/L as determined by surface plasmon resonance sensorgram (Supplementary Fig. S2A). No degradation of ^{64}Cu-labeled c(TNYL-RAW) was observed by high-performance liquid chromatography after incubation of the peptide in mouse plasma over a period of 24 hours, whereas ^{64}Cu-labeled linear TNYL-RAW was degraded as soon as 2 hours after incubation (Supplementary Fig. S2B). c(TNYL-RAW) was linked to SATA-PEG-NHS through an activated ester. After deprotection of the SH group, SH-PEG-c(TNYL-RAW) was conjugated to HAuNS in an aqueous solution via S-Au bonding (Fig. 1). The amount of c(TNYL-RAW) conjugated to the HAuNS was determined by quantitative amino acid analysis after complete dissolution of c(TNYL-RAW)-conjugated HAuNS. The conjugation efficiency was 13.7% and there were about 880 molecules of c(TNYL-RAW) on each HAuNS nanoparticle. DOX was readily loaded into c(TNYL-RAW)-conjugated HAuNS using a previously reported method to give T-DOX@HAuNS (5). DOX loading efficiency was over 90%, and DOX content was 30% (w/w).

In vitro uptake in cancer cells

Next, we evaluated the selectivity of uptake of c(TNYL-RAW)-conjugated DOX@HAuNS in EphB4-positive tumor cells. Western blotting indicated high expression levels of EphB4 receptor in MBA-MD-231, A2780, and Hey cells, but only low expression level in A549 cells (Supplementary Fig. S3A). Immunostaining using anti-EphB4 antibody confirmed strong EphB4 signals from A2780, MDA-MB-231, and Hey cells but weak signal from A549 cells (Supplementary Fig. S3B). On the basis of these findings, we selected the Hey tumor for subsequent efficacy studies.

Figure 2A shows representative photomicrographs of fluorescence and dark-field images of Hey cells incubated with T-DOX@HAuNS. The nanoparticles were readily taken up by the tumor cells. The fluorescence signal from the DOX was colocalized with the signal from the HAuNS, indicating that the DOX remained associated with the HAuNS after T-DOX@HAuNS were internalized. Under the same conditions, significantly more T-DOX@HAuNS was internalized in the cells with high EphB4 receptor expression (Hey) than in the cells with low EphB4 receptor expression (A549; $P<0.05$, Fig. 2B). The addition of free c(TNYL-RAW) peptide into the culture medium (Hey cells) induced a significant decrease in the cellular uptake of the nanoparticles ($P < 0.005$) but did not cause a change in uptake in the A549 cells that had low EphB4 receptor

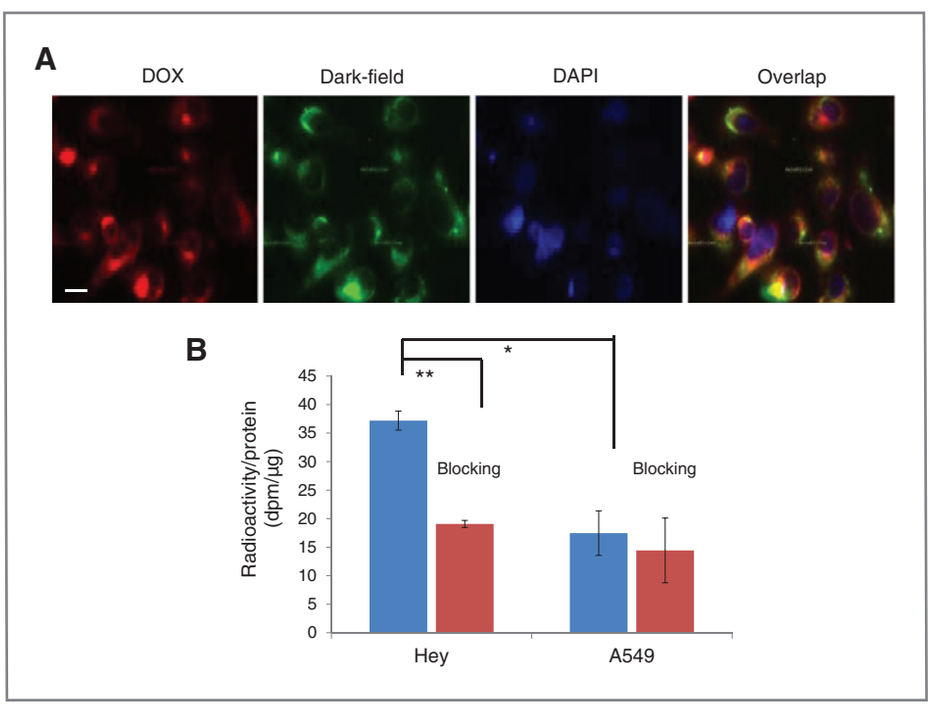

Figure 2. Cellular uptake of T-DOX@HAuNS. A, representative photomicrographs of Hey cells after incubation with T-DOX@HAuNS for 2 hours. The scattering signal from the HAuNS was visualized using a dark-field condenser (green), and red fluorescence was from DOX. Cell nuclei were counterstained with 4′, 6-diamidino-2-phenylindole (blue). Bar, 20 μm. B, quantitative cellular uptake of nanoparticles in Hey and A549 cells after 3 hours incubation with ^{111}In-labeled T-DOX@HAuNS and T-DOX@HAuNS plus free c (TNYL-RAW) (blocking). **, $P < 0.005$; *, $P < 0.05$.

expression (Fig. 2B). These data indicate that T-DOX@HAuNS was taken up by EphB4-positive cells via receptor-mediated endocytosis.

Cytotoxicity

For cells with low EphB4 expression (A549), the difference in cytotoxicity between T-DOX@HAuNS and nontargeted DOX@HAuNS was minimal, demonstrating the importance of EphB4-mediated uptake (Supplementary Fig. S4A). Free DOX exhibited higher toxicity in A549 cells than both T-DOX@HAuNS and DOX@HAuNS. The lower cytotoxic potency of T-DOX@HAuNS and DOX@HAuNS can be attributed to relatively stable complexes formed between DOX and HAuNS and delayed DOX release inside cells. However, significantly higher toxicity was shown for T-DOX@HAuNS in A2780 cells than either free DOX or DOX@HAuNS (Supplementary Fig. S4B). The higher cellular cytotoxicity with targeted nanoparticles can be attributed to the increased uptake of T-DOX@HAuNS in the target cells.

Pharmacokinetics, biodistribution, and SPECT imaging

Figure 3A shows the mean blood activity time profile of ^{111}In-labeled T-DOX@HAuNS and DOX@HAuNS. The pharmacokinetic parameters are summarized in Table 1. DOX@HAuNS had moderately higher area under the blood drug concentration–time curve extrapolated to infinite time ($AUC_{0-\infty}$, 322.3%ID h/mL ± 72%ID h/mL) than T-DOX@HAuNS (242.8%ID h/mL ± 46%ID h/mL, $P = 0.046$). However, there was no significant difference between the 2 HAuNS formulations in any other pharmacokinetic parameters ($P \geq 0.05$), suggesting that the conjugation of c(TNYL-RAW) to HAuNS did not significantly change the pharmacokinetic properties of the nanoparticles. Both types of nanoparticles (T-DOX@HAuNS and DOX@HAuNS) were almost completely eliminated from the blood at 48 hours after injection. Figure 3B shows the biodistribution of T-DOX@HAuNS, T-DOX@HAuNS with blocking by free c(TNYL-RAW), and DOX@HAuNS in nude mice at 24 hours after injection. Most nanoparticles were taken up by the liver, spleen, and kidney. Interestingly, significantly less T-DOX@HAuNS than DOX@HAuNS accumulated in the liver ($P = 0.0009$) and the spleen ($P = 0.0006$). Conversely, T-DOX@HAuNS had significantly higher uptake in the kidney than DOX@HAuNS did ($P = 0.004$). With the exception of kidney uptake, coinjection with an excess of c(TNYL-RAW) did not affect the biodistribution pattern of T-DOX@HAuNS. c(TNYL-RAW) blocking reduced the kidney uptake of T-DOX@HAuNS from 17.2%ID/g to 12.9%ID/g ($P = 0.02$). This finding may be reflective of EphB4 expression in venous endothelium of the kidney (20).

To show efficiency of tumor targeting, we next carried out biodistribution studies in tumor-bearing mice. T-DOX@HAuNS displayed significantly higher accumulation than nontargeted DOX@HAuNS in tumors with high EphB4 receptor expression, with 3.0-, 2.1-, and 1.6-fold mean increases in Hey ($P = 0.0016$), A2780 ($P = 0.0005$), and MDA-MB-231

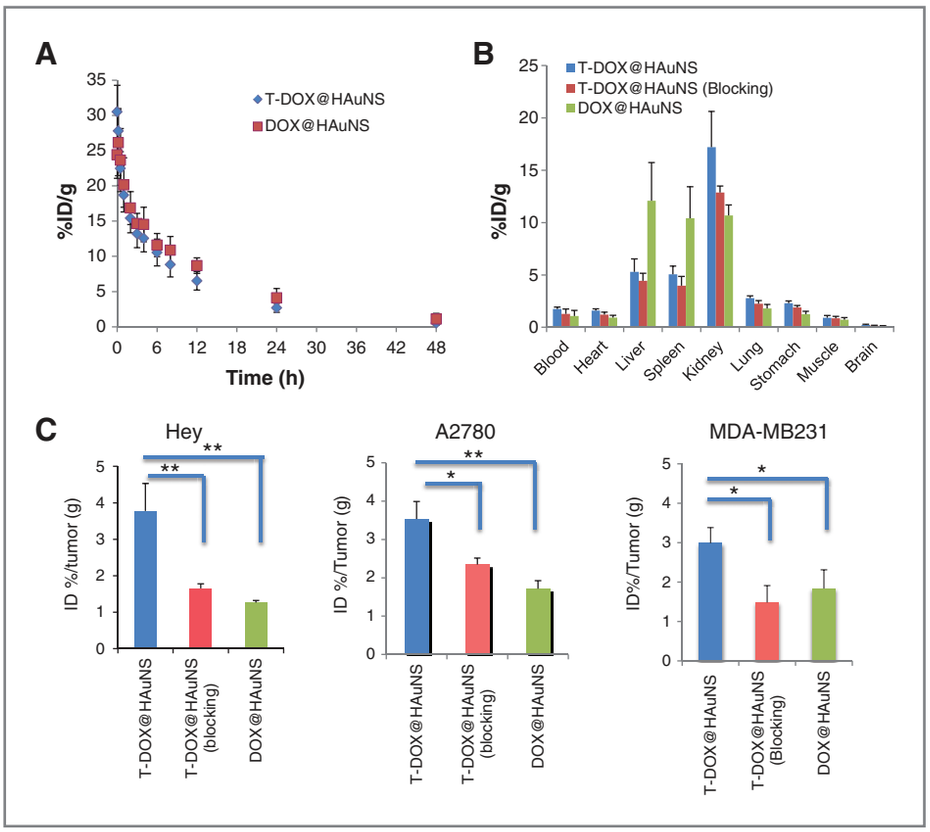

Figure 3. T-DOX@HAuNS pharmacokinetics, biodistribution, and tumor uptake. A, activity–time profiles of ^{111}In-labeled T-DOX@HAuNS and DOX@HAuNS in Swiss mice. The data are expressed as percentage of the injected dose per gram of blood (%ID/g) and are presented as mean ± SD ($n = 8$). B, biodistribution of ^{111}In-labeled T-DOX@HAuNS, T-DOX@HAuNS with blocking, and DOX@HAuNS in nude mice at 24 hours after injection. C, comparison of nanoparticle uptake in Hey, A2780, and MDA-MB-231 tumors at 24 hours postinjection. The data are expressed as percentage of the injected dose per gram of tissue (%ID/g) and are presented as mean ± SD ($n = 6$). **, $P < 0.005$; *, $P < 0.05$.

Table 1. Pharmacokinetic parameters of DOX@HAuNS and T-DOX@HAuNS after intravenous injection in female Swiss mice

PK parameters	DOX@HAuNS	T-DOX@HAuNS	*P*
Elimination half-life, h	11.9 ± 3.8	9.75 ± 1.7	0.229
C_{max}, %ID/mL	28.9 ± 4.9	30.8 ± 3.7	0.459
$AUC_{0-\infty}$, %ID h/mL	322.3 ± 72	242.8 ± 46	0.046
CL, mL/h	0.323 ± 0.068	0.426 ± 0.092	0.050
V_d, mL	5.30 ± 0.81	5.85 ± 0.69	0.239
V_{ss}, mL	4.94 ± 0.70	5.25 ± 0.61	0.439
MRT, h	16.0 ± 5.0	12.6 ± 1.8	0.137

NOTE: ANOVA showed no differences between the 2 HAuNS formulations.

Abbreviations: $AUC_{0-\infty}$, area under the blood drug concentration–time curve extrapolated to infinite time; C_{max}, maximum blood concentration; CL, systemic clearance; MRT, mean residence time; V_d, volume of distribution; V_{ss}, volume of distribution at steady state.

tumors ($P = 0.019$), respectively (Fig. 3C). Furthermore, the addition of free c(TNYL-RAW) peptide significantly reduced the uptake of T-DOX@HAuNS in these tumors, with 2.3-, 1.5-, and 2.0-fold decreases, respectively (Fig. 3C). These results indicated that T-DOX@HAuNS was actively targeted to tumors expressing EphB4.

SPECT images showed significant blood activity in the liver and spleen for both ^{111}In-labeled T-DOX@HAuNS and DOX@HAuNS (Fig. 4). By 24 hours after injection, accumulation of T-DOX@HAuNS in the tumor was clearly visualized (Fig. 4A). The uptake of T-DOX@HAuNS in the Hey tumors was blocked by an excess of free c(TNYL-RAW) (Fig. 4B). Similarly, tumor uptake of then nontargeted DOX@HAuNS was barely visible (Fig. 4C). Autoradiographs of all 3 tumors (Hey, A2780, and MDA-MB-231) showed stronger ^{111}In radioactivity signals with T-DOX@HAuNS than with T-DOX@HAuNS plus free c (TNYL-RAW) or with DOX@HAuNS (Fig. 4D).

In vivo antitumor activity

The temperature measured by the thermocouple within the tumor reached approximately 53°C after 5 minutes of NIR laser exposure on the tumor surface at an output power of 3 W/cm^2 in mice injected with T-DOX@HAuNS (Fig. 5A). No change in temperature was noted under the same conditions in the tumors of control mice. Dual-tracer autoradiography showed that immediately after NIR laser irradiation, ^{3}H-DOX was released and dispersed into the area surrounding the site where T-DOX@HAuNS was introduced. Conversely, ^{3}H-DOX was mostly colocalized with ^{111}In-HAuNS in mice that did not undergo NIR laser treatment (Fig. 5B).

Figure 6A shows the Hey tumor growth curves after intravenous injections of saline, HAuNS [5.0 mL/kg of 1.25 mg HAuNS/mL saline (50 OD), no DOX, no targeting], DOX@HAuNS (10 mg equivalent DOX/kg, 5.0 mL/kg of 1.25 mg HAuNS/mL), and T-DOX@HAuNS (10 mg equivalent DOX/kg, 5.0 mL/kg of 1.25 mg HAuNS/mL). Mice in each group received NIR laser treatment (2.0 W/cm^2 for 3 minutes) 24 hours after injection. The mice in the saline plus laser group were killed on day 9 after injection because most of the tumors in this group were approximately 1500 mm^3 at that time. Mice in the other 3 groups were killed on day 22. Treatment with T-DOX@HAuNS plus laser showed

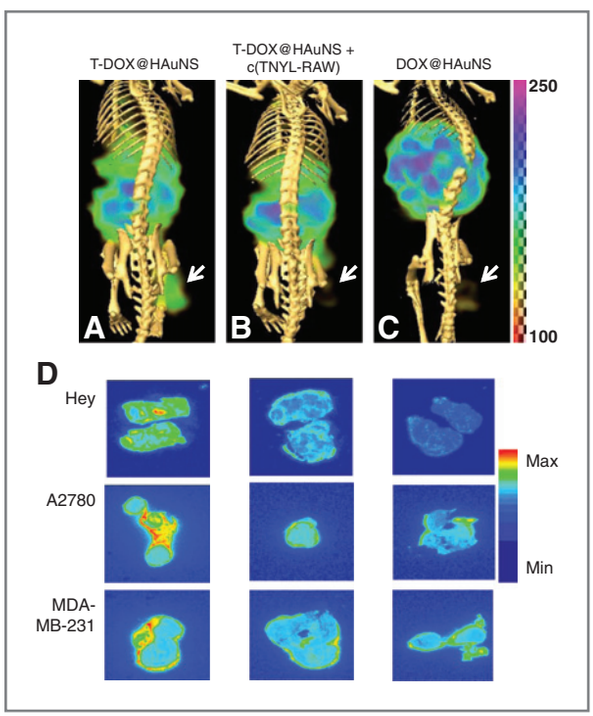

Figure 4. microSPECT/CT imaging and autoradiography of ^{111}In-labeled T-DOX@HAuNS and DOX@HAuNS. A–C, representative SPECT images of nude mice bearing Hey tumors at 24 hours after intravenous injection of ^{111}In-labeled T-DOX@HAuNS, ^{111}In-labeled T-DOX@HAuNS plus free c (TNYL-RAW), and ^{111}In-labeled DOX@HAuNS. Arrows indicate tumors. D, representative autoradiographs of slices sectioned from Hey, A2780, and MDA-MB-231 tumors at 24 hours after injection. Stronger signals were visualized for tumors imaged after the injection of ^{111}In-labeled T-DOX@HAuNS than of T-DOX@HAuNS plus free c(TNYL-HAuNS) or DOX@HAuNS.

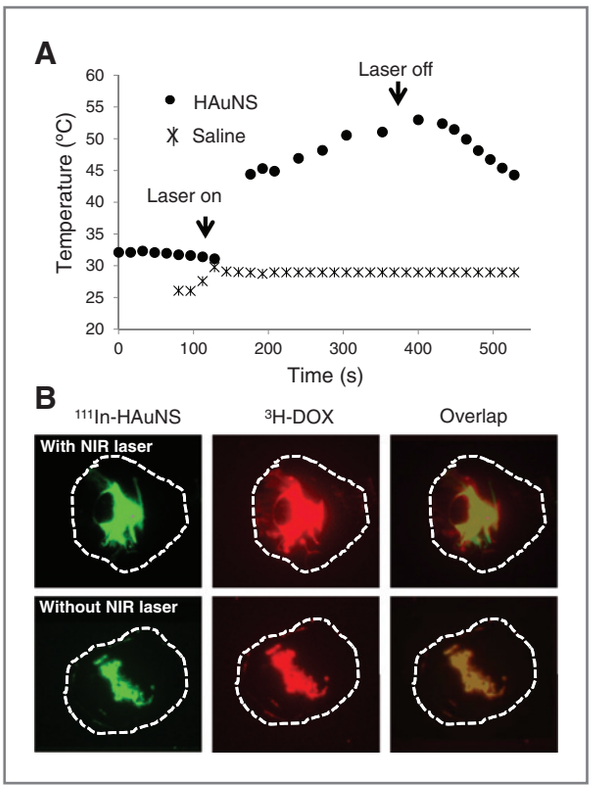

Figure 5. *In vivo* release of DOX upon NIR treatment. A, NIR-induced temperature change in tumors injected with HAuNS. B, DOX release from T-DOX@HAuNS in tumors treated with NIR laser irradiation. The white broken circle indicates the tumor outline. Green (^{111}In-HAuNS) and red (^{3}H-DOX) signals indicate the location of the HAuNS and DOX, respectively.

significantly enhanced antitumor activity compared with saline plus laser, HAuNS plus laser, and DOX@HAuNS plus laser. The mean tumor weight in T-DOX@HAuNS plus laser group on day 22 after treatment was 0.0038 ± 0.0007 g (n = 8), which was significantly smaller than that of the saline plus laser (1.2 ± 0.51 g on day 9, n = 6; P<0.0001), HAuNS plus laser (1.5 ± 0.34 g on day 22, n = 6; P<0.0001), and DOX@HAuNS plus laser (0.36 ± 0.24 g on day 22, n = 7; P<0.001) groups (Fig. 6B). The tumors in this group of mice became whitish immediately after treatment, suggesting disruption of blood perfusion. Remarkably, the tumors in 6 of the 8 mice treated with T-DOX@HAuNS plus laser regressed completely and became scar tissue by 22 days after the injection. Histologic analysis showed the presence of scar tissue and a lack of residual tumor cells in mice treated with T-DOX@HAuNS plus laser (Fig. 6C). Tumors in the nontargeted DOX@HAuNS plus laser group became loose and discrete, suggesting damage to tumor cells. However, tumors could not be completely eradicated without targeting ligand. Tumors in the saline plus laser group appeared to be intact. In the saline plus laser and DOX@HAuNS plus laser treatment groups, viable tumor cells were found throughout the tumor volumes (Fig. 6C). No apparent signs of toxicity were observed throughout the course of the study. The body weight of mice in all treatment groups steadily increased during the study period (Supplementary Fig. S5).

Discussion

In this study, we showed that T-DOX@HAuNS had significantly greater cytotoxic effects in tumor cells with high EphB4 receptor expression than DOX@HAuNS and free DOX did *in vitro*. Moreover, T-DOX@HAuNS showed enhanced antitumor activity when combined with NIR laser irradiation than DOX@HAuNS plus laser treatment *in vivo*. These findings indicate that c(TNYL-RAW) peptide is highly effective for selective delivery of T-DOX@HAuNS to tumors with high expression of EphB4. The significantly enhanced antitumor activity of T-DOX@HAuNS could be attributed to (i) increased accumulation of the nanoparticles in tumors, (ii) controlled release of DOX mediated by NIR laser irradiation, and (iii) synergistic interaction between chemotherapy and PTA therapy, both of which were activated concurrently by NIR laser.

In our nanoconstruct, c(TNYL-RAW) peptide with high EphB4 binding affinity and high plasma stability was conjugated to HAuNS through a PEG linker, which ensured availability of the peptide to the target receptor (Fig. 1). This strategy has been successfully used for the formulation of other targeted nanoparticles by us and others (4, 21–24). Additional monofunctional SH-PEG chains were introduced together with SH-PEG-c(TNYL-RAW) to ensure that all available gold surface was covered by PEG. This process was used to create DOX@HAuNS and ligand-conjugated T-DOX@HAuNS, both of which had high colloidal stability.

Both *in vitro* and *in vivo* data showed that tumor uptake of T-DOX@HAuNS could be partially blocked by free c(TNYL-RAW) peptide, confirming that cell uptake of T-DOX@HAuNS was mediated by EphB4 (Figs. 2–4). *In vivo*, T-DOX@HAuNS displayed significantly higher accumulation than nontargeted DOX@HAuNS in all 3 tumor models evaluated. Because DOX@HAuNS and T-DOX@HAuNS exhibited similar pharmacokinetic behaviors (Fig. 3A, Table 1), the difference in tumor uptake between targeted and nontargeted HAuNS is unlikely a result of enhanced permeability and retention effect. Hence, our data support successful EphB4 receptor–mediated targeted delivery of T-DOX@HAuNS after intravenous injection.

In addition to active targeting mediated by receptor ligands exemplified in this study, physiologic and physical methods such as tumor priming, vascular disruption, degradation of the extracellular matrix, and vessel normalization may be used to improve tumor distribution of nanoparticles (25–29). Recent studies have shown that losartan, a clinically approved angiotensin II receptor antagonist, is an effective agent for normalizing tumor vasculature (29). Losartan inhibited collagen I production by tumor-associated fibroblasts, which led to a dose-dependent reduction in stromal collagen in several human tumor xenograft models. As a result, the drug enhanced the delivery and efficacy of intravenously injected pegylated liposomal doxorubicin (Doxil). These studies suggest that targeted nanoparticles such as T-DOX@HAuNS may achieve further improvement in tumor deposition when combined with physiological and physical approaches.

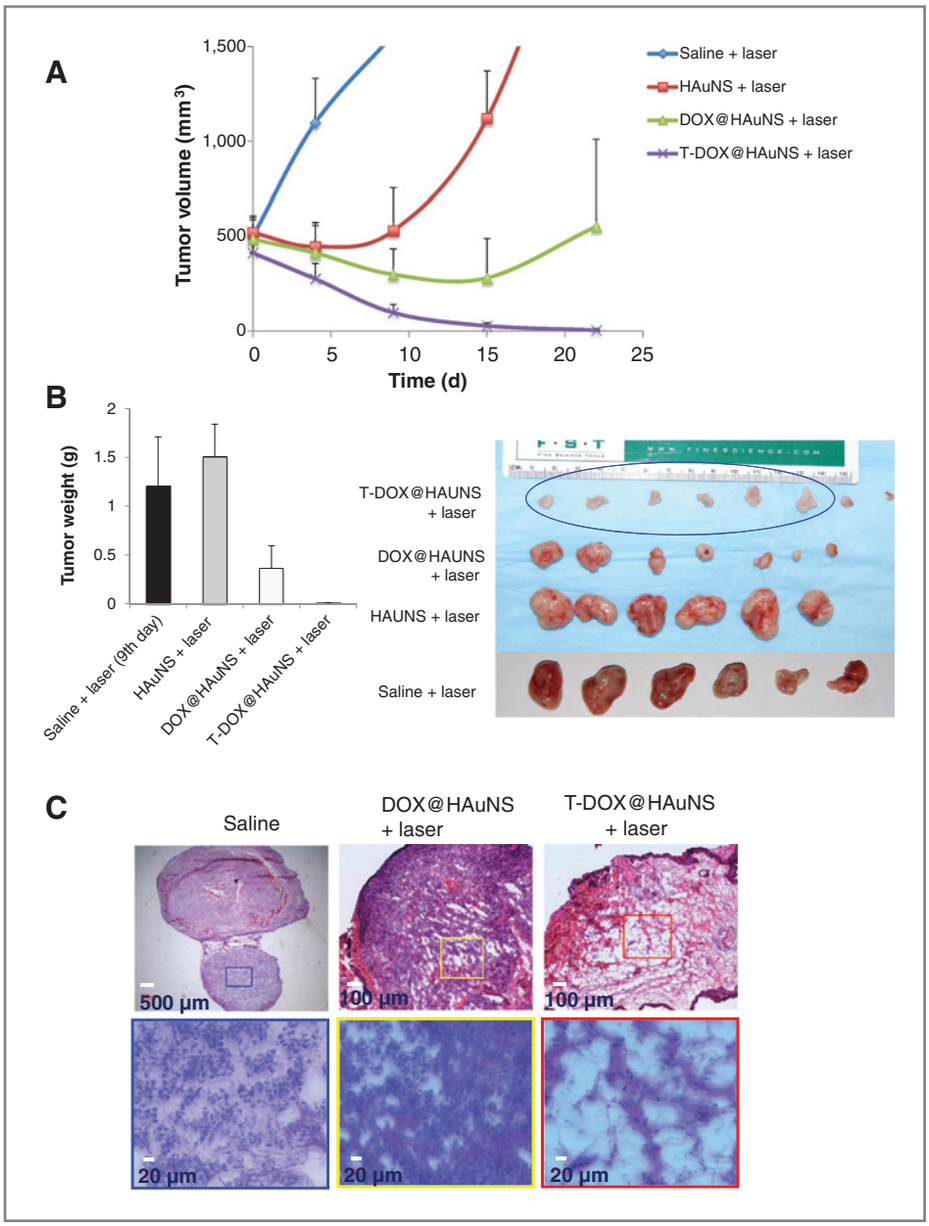

Figure 6. Antitumor activity of various treatments against Hey tumors. A, tumor growth curves for mice treated with saline plus laser ($n = 6$), HAuNS plus laser ($n = 6$), DOX@HAuNS plus laser ($n = 7$), and T-DOX@HAuNS plus laser ($n = 8$). NIR laser irradiation (2.0 W/cm^2 for 3 minutes) was commenced at 24 hours after injection. B, average tumor weights (left) and photographs (right) of tumors from different treatment groups. Tumors were removed on day 22 for all groups except the saline plus laser group, in which tumors were removed on day 9. Six tumors in the T-DOX@HAuNS group regressed completely by day 22 after treatment, and only the scar tissues at the site of tumor inoculation were removed and photographed (blue circle, right). C, representative photomicrographs of hematoxylin and eosin–stained slides from scar tissue from a mouse treated with T-DOX@HAuNS plus laser or tumors from mice treated with saline or DOX@HAuNS plus laser on day 22 after treatment.

The temperature in tumors of mice received intravenous injection of T-DOX@HAuNS reached approximately 53°C after 5 minutes of continuous wave NIR laser exposure at 3 W/cm^2 (Fig. 5A). This temperature is sufficient for causing irreversible damage to cancer cells (30). As expected, there was no temperature change in the tumors of mice that did not receive the nanoparticle injection followed by NIR irradiation. Therefore, T-DOX@HAuNS medicated efficient photothermal effect. We have previously shown that in aqueous solution, the release of DOX from DOX@HAuNS could be activated by NIR laser irradiation (5). To show that DOX could be released *in vivo* upon NIR irradiation, we used an autoradiographic technique with dual-radiotracer labeling. ^{3}H undergoes beta decay with a 12.3-year half-life, releasing 18.6 keV of energy in the process. On the other hand, ^{111}In emits gamma radiation with a half-life of 2.81 days at much higher energy (171 and 245 KeV). Taking advantage of these differences in the decay properties between ^{3}H and ^{111}In, we were able to separate signals from HAuNS and DOX in the tumors. Thus, immediately after NIR laser irradiation at 3 W/cm^2, ^{3}H-DOX was dissociated from ^{111}In-HAuNS, whereas in the control tumor not exposed to NIR laser irradiation, signals from ^{3}H-DOX colocalized perfectly with ^{111}In-HAuNS (Fig. 6B). These data confirm that free DOX was released from T-DOX@HAuNS and then diffused away from the nanoparticles when tumors were exposed to the NIR laser.

The antitumor efficacy of free DOX, DOX@HAuNS, DOX@HAuNS plus NIR laser was investigated against MDA-MB-231 tumors in our previous work (31). There was no significant difference in tumor size between groups treated with DOX (15 mg/kg, 1 injection) and DOX@HAuNS (15 mg

equivalent DOX/kg per injection, 2 injections). However, DOX@HAuNS plus NIR laser (15 mg equivalent DOX/kg per injection, 2 injections) reduced tumor volume significantly more than the other 2 treatments (31). In these studies, free DOX at a single dose of 15 mg/kg caused serious systemic toxicity and cardiotoxicity. Therefore, we did not use free DOX as a control in the current study. Instead, we used nontargeted DOX@HAuNS as a control and compared the antitumor studies of T-DOX@HAuNS against ovarian Hey tumors with that of DOX@HAuNS. Combined T-DOX@HAuNS plus laser treatments showed significantly better antitumor activity than combined HAuNS plus laser (PTA only) and nontargeted DOX@HAuNS plus laser treatments (Fig. 6).

Significantly, this higher antitumor activity was achieved without causing significant systemic toxicity, as indicated by continued increase in body weight in mice in all treatment groups (Supplementary Fig. S5). In our previous work, we compared the toxicity of free DOX, liposomal DOX, and DOX@HAuNS (31). DOX@HAuNS after a single dose at 60 mg equivalent DOX/kg had no cardiotoxicity compared with liposomal DOX (2 doses at a total dose of 30 mg DOX/kg) and free DOX (single dose of 15 mg/kg). In the heart, 100% of both liposomal DOX- and free DOX–treated mice had a vacuolar cardiomyopathy. However, for mice treated with DOX@HAuNS, the histopathologic features in the heart were similar to those observed in the saline-treated control mice and no abnormal features were observed. Because DOX@HAuNS and T-DOX@HAuNS had similar pharmacokinetic properties and there was no significant different in heart accumulation between the 2 agents, we expect that T-DOX@HAuNS will display toxicity profile similar to that of DOX@HAuNS. Further studies are required to document both short- and long-term systemic toxicity of T-DOX@HAuNS after intravenous injection.

Our study has several limitations. First, *in vivo* release of DOX upon laser irradiation was conducted after intratumoral injection, which may not accurately reflect DOX distribution that will be seen after systemic administration, followed by NIR treatment. However, the sole purpose of this experiment was to examine whether DOX release can be triggered by NIR laser irradiation under *in vivo* conditions, which was confirmed in the current study. Second, we did not analyze the distribution of DOX when DOX@HAuNS and T-DOX@HAuNS were given intravenously. Detailed DOX biodistribution in comparison to HAuNS after systemic administration of nontargeted DOX@HAuNS has been studied and published in our previous work using a dual-radiotracer technique (31). It was found that DOX@HAuNS was stable in the blood during the first 6 hours after injection. By 24 hours after injection, there was disparity in biodistribution pattern between DOX and HAuNS, indicating gradual release of DOX from DOX@HAuNS.

A potential limitation of the proposed concurrent chemo-photothermal therapy strategy is penetration depth of NIR light. The current state-of-the-art enables NIR light to penetrate up to 1 to 2 cm in soft tissue (32). With the newer 10- to 40-mm long quartz laser fibers and water-cooled laser application sheaths, ablative areas of 50 to 80 mm have been achieved (33–35). Deeper reach is also possible with various minimally invasive interventional techniques, such as endoscopic, intravascular, and percutaneous approaches. Currently, laser beam is delivered through laser fibers inserted into the tumors, as in the case of primary and metastatic liver cancer (33, 35, 36) and lung metastases (37). In our previous work, we evaluated the triggered release of paciltaxel via NIR laser irradiation and its antitumor efficacy by hepatic arterial administration of HAuNS- and paclitaxel-loaded microspheres into rabbits with liver carcinoma *in situ* (38). The results showed that NIR laser irradiation after the microspheres administration results in intratumoral heating. NIR laser irradiation can trigger release of paclitaxel from the microspheres, and can potentially increase the efficacy of treatment after hepatic arterial delivery of the microspheres in liver tumors. Thus, we believe that chemo-photothermal therapy approach entailed in this work is best suited for unresectable, locally advanced disease that ultimately causes patient death. It is envisioned that chemo-PTA therapy may also be used in conjunction with surgery, especially used in postsurgery setting to eradicate residual tumor cells. In such as case, the laser beam can be conveniently delivered through surface exposure.

Disclosure of Potential Conflict of Interest

No potential conflicts of interest were disclosed.

Authors' Contributions

Conception and design: J. You, C. Xiong, M. Zhong, S. Gupta, A.K. Sood, C. Li
Development of methodology: J. You, C. Xiong, S. Gupta, C. Li
Acquisition of data (provided animals, acquired and managed patients, provided facilities, etc.): J. You, M. Melancon, C. Li
Analysis and interpretation of data (e.g., statistical analysis, biostatistics, computational analysis): J. You, C. Xiong, S. Gupta, A.K. Sood, C. Li
Writing, review, and/or revision of the manuscript: J. You, M. Melancon, S. Gupta, A.M. Nick, A.K. Sood, C. Li
Administrative, technical, or material support (i.e., reporting or organizing data, constructing databases): M. Zhong, M. Melancon, A.K. Sood

Grant Support

This work was supported in part by NIH grants RC2 GM092599, Center of Cancer Nanotechnology Excellence grant (U54 CA151668), the John S. Dunn Foundation, and the National Nature Science Foundation of PR China (81001411). The authors thank the NCI Cancer Center Support Grant CA016672, which supports MD Anderson's Small Animal Imaging Facility and TEM Core Facility.

The costs of publication of this article were defrayed in part by the payment of page charges. This article must therefore be hereby marked *advertisement* in accordance with 18 U.S.C. Section 1734 solely to indicate this fact.

Received March 21, 2012; revised May 8, 2012; accepted June 1, 2012; published OnlineFirst August 3, 2012.

References

1. Bardhan R, Lal S, Joshi A, Halas NJ. Theranostic nanoshells: from probe design to imaging and treatment of cancer. Acc Chem Res 2011;44:936–46.

2. Melancon M, Lu W, Li C. Gold-based magneto/optical nanostructures: challenges for *in vivo* applications in cancer diagnostics and therapy. Mater Res Bull 2009;34:415–21.

3. Melancon MP, Lu W, Yang Z, Zhang R, Cheng Z, Elliot AM, et al. *In vitro* and *in vivo* targeting of hollow gold nanoshells directed at epidermal growth factor receptor for photothermal ablation therapy. Mol Cancer Ther 2008;7:1730–9.
4. Lu W, Xiong C, Zhang G, Huang Q, Zhang R, Zhang JZ, et al. Targeted photothermal ablation of murine melanomas with melanocyte-stimulating hormone analog-conjugated hollow gold nanospheres. Clin Cancer Res 2009;15:876–86.
5. You J, Zhang G, Li C. Exceptionally high payload of doxorubicin in hollow gold nanospheres for near-infrared light-triggered drug release. ACS Nano 2010;4:1033–41.
6. Pasquale EB. Eph receptor signalling casts a wide net on cell behaviour. Nat Rev Mol Cell Biol 2005;6:462–75.
7. Dodelet VC, Pasquale EB. Eph receptors and ephrin ligands: embryogenesis to tumorigenesis. Oncogene 2000;19:5614–9.
8. Nakamoto M, Bergemann AD. Diverse roles for the Eph family of receptor tyrosine kinases in carcinogenesis. Microsc Res Tech 2002;59:58–67.
9. Walker-Daniels J, Hess AR, Hendrix MJ, Kinch MS. Differential regulation of EphA2 in normal and malignant cells. Am J Pathol 2003; 162:1037–42.
10. Brantley-Sieders DM, Caughron J, Hicks D, Pozzi A, Ruiz JC, Chen J. EphA2 receptor tyrosine kinase regulates endothelial cell migration and vascular assembly through phosphoinositide 3-kinase-mediated Rac1 GTPase activation. J Cell Sci 2004;117:2037–49.
11. Noren NK, Lu M, Freeman AL, Koolpe M, Pasquale EB. Interplay between EphB4 on tumor cells and vascular ephrin-B2 regulates tumor growth. Proc Natl Acad Sci U S A 2004;101:5583–8.
12. Battaglia AA, Sehayek K, Grist J, McMahon SB, Gavazzi I. EphB receptors and ephrin-B ligands regulate spinal sensory connectivity and modulate pain processing. Nat Neurosci 2003;6:339–40.
13. Goldshmit Y, Galea MP, Wise G, Bartlett PF, Turnley AM. Axonal regeneration and lack of astrocytic gliosis in EphA4-deficient mice. J Neurosci 2004;24:10064–73.
14. Xia G, Kumar SR, Stein JP, Singh J, Krasnoperov V, Zhu S, et al. EphB4 receptor tyrosine kinase is expressed in bladder cancer and provides signals for cell survival. Oncogene 2006;25:769–80.
15. Koolpe M, Burgess R, Dail M, Pasquale EB. EphB receptor-binding peptides identified by phage display enable design of an antagonist with Ephrin-like affinity. J Biol Chem 2005;280:17301–11.
16. Erber R, Eichelsbacher U, Powajbo V, Korn T, Djonov V, Lin JH, et al. EphB4 controls blood vascular morphogenesis during postnatal angiogenesis. EMBO J 2006;25:628–41.
17. Kumar SR, Scehnet JS, Ley EJ, Singh J, Krasnoperov V, Liu R, et al. Preferential induction of EphB4 over EphB2 and its implication in colorectal cancer progression. Cancer Res 2009;69:3736–45.
18. Kumar SR, Singh J, Xia GB, Krasnoperov V, Hassanieh L, Ley EJ, et al. Receptor tyrosine kinase EphB4 is a survival factor in breast cancer. Am J Pathol 2006;169:279–93.
19. Xiong C, Huang M, Zhang R, Song S, Lu W, Flores L II, et al. *In vivo* small-animal PET/CT of EphB4 receptors using 64Cu-labeled peptide. J Nucl Med 2011;52:241–8.
20. Ozgur E, Heidenreich A, Dagtekin O, Engelmann U, Bloch W. Distribution of EphB4 and EphrinB2 in normal and malignant urogenital tissue. Urol Oncol 2011;29:78–84.
21. Wang X, Qian X, Beitler JJ, Chen ZG, Khuri FR, Lewis MM, et al. Detection of circulating tumor cells in human peripheral blood using surface-enhanced Raman scattering nanoparticles. Cancer Res 2011;71:1526–32.
22. Davis ME, Zuckerman JE, Choi CH, Seligson D, Tolcher A, Alabi CA, et al. Evidence of RNAi in humans from systemically administered siRNA via targeted nanoparticles. Nature 2010;464:1067–70.
23. Petros RA, DeSimone JM. Strategies in the design of nanoparticles for therapeutic applications. Nat Rev Drug Discov 2010;9:615–27.
24. Lu W, Zhang G, Zhang R, Flores LG II, Huang Q, Gelovani JG, et al. Tumor site-specific silencing of NF-kappa B p65 by targeted hollow gold nanosphere-mediated photothermal transfection. Cancer Res 2010;70:3177–88.
25. Lu D, Wientjes MG, Lu Z, Au JL. Tumor priming enhances delivery and efficacy of nanomedicines. J Pharmacol Exp Ther 2007;322:80–8.
26. Melancon MP, Elliott A, Ji X, Shetty A, Yang Z, Tian M, et al. Theranostics with multifunctional magnetic gold nanoshells: photothermal therapy and t2* magnetic resonance imaging. Invest Radiol 2011;46: 132–40.
27. Eikenes L, Tari M, Tufto I, Bruland OS, de Lange Davies C. Hyaluronidase induces a transcapillary pressure gradient and improves the distribution and uptake of liposomal doxorubicin (Caelyx) in human osteosarcoma xenografts. Br J Cancer 2005;93:81–8.
28. Eikenes L, Bruland OS, Brekken C, Davies Cde L. Collagenase increases the transcapillary pressure gradient and improves the uptake and distribution of monoclonal antibodies in human osteosarcoma xenografts. Cancer Res 2004;64:4768–73.
29. Diop-Frimpong B, Chauhan VP, Krane S, Boucher Y, Jain RK. Losartan inhibits collagen I synthesis and improves the distribution and efficacy of nanotherapeutics in tumors. Proc Natl Acad Sci U S A 2011;108: 2909–14.
30. Melancon MP, Zhou M, Li C. Cancer theranostics with near-infrared light-activatable multimodal nanoparticles. Acc Chem Res 2011;44: 947–56.
31. You J, Zhang R, Zhang G, Zhong M, Liu Y, Van Pelt CS, et al. Photothermal-chemotherapy with doxorubicin-loaded hollow gold nanospheres: a platform for near-infrared light-trigged drug release. J Control Release 2012;158:319–28.
32. Gu Y, Chen WR, Xia M, Jeong SW, Liu H. Effect of photothermal therapy on breast tumor vascular contents: noninvasive monitoring by near-infrared spectroscopy. Photochem Photobiol 2005;81: 1002–9.
33. Gough-Palmer AL, Gedroyc WM. Laser ablation of hepatocellular carcinoma—a review. World J Gastroenterol 2008;14:7170–4.
34. Muralidharan V, Malcontenti-Wilson C, Christophi C. Interstitial laser hyperthermia for colorectal liver metastases: the effect of thermal sensitization and the use of a cylindrical diffuser tip on tumor necrosis. J Clin Laser Med Surg 2002;20:189–96.
35. Vogl TJ, Straub R, Zangos S, Mack MG, Eichler K. MR-guided laser-induced thermotherapy (LITT) of liver tumours: experimental and clinical data. Int J Hyperthermia 2004;20:713–24.
36. Vogl TJ, Straub R, Eichler K, Sollner O, Mack MG. Colorectal carcinoma metastases in liver: laser-induced interstitial thermotherapy—local tumor control rate and survival data. Radiology 2004; 230:450–8.
37. Rosenberg C, Puls R, Hegenscheid K, Kuehn J, Bollman T, Westerholt A, et al. Laser ablation of metastatic lesions of the lung: long-term outcome. Am J Roentgenol 2009;192:785–92.
38. Gupta S, Stafford RJ, Javadi S, Ozkan E, Ensor JE, Wright KC, et al. Effects of near-infrared laser irradiation of biodegradable microspheres containing hollow gold nanospheres and paclitaxel administered intraarterially in a rabbit liver tumor model. J Vasc Interv Radiol 2012;23:553–61.